ELSEVIER

Contents lists available at ScienceDirect

Fuel Processing Technology

journal homepage: www.elsevier.com/locate/fuproc





Flash-pyrolyzed coal char as a high-performance anode for sodium-ion batteries

Jaron V. Moon a,* , Zahra Karimi a , Alex Prlina b , Chanel Van Ginkel a , Danielle M. Horlacher a , Eric G. Eddings b , Roseanne Warren a

- a Department of Mechanical Engineering, University of Utah, 1495 E 100 S, Salt Lake City, UT 84112, United States of America
- b Department of Chemical Engineering, University of Utah, Merrill Engineering, 50 Central Campus Dr, Salt Lake City, UT 84112, United States of America

ARTICLE INFO

Keywords:
Sodium-ion batteries
Coal char
Flash pyrolysis
Ether-based electrolyte
Small-angle X-ray scattering

ABSTRACT

This work explores a novel approach for improving the sodium-ion battery performance of coal char using flash pyrolysis and an ether-based electrolyte. Coal char is an ultra-low cost hard carbon with promising application as an anode material in sodium-ion batteries. During flash pyrolysis, char is heated at $1000\,^{\circ}$ C/s in a drop-tube furnace to create a highly-irregular structure. The larger d-spacing and smaller closed micropore diameter of flash-pyrolyzed char increases anode capacity compared to traditional slow-pyrolyzed char electrodes. The sodium-ion battery anode performance of flash-pyrolyzed char is further improved using an ether-based electrolyte in place of the traditional ester-based electrolyte. Performance improvements include greater initial Coulombic efficiency (58% in ester- vs. 64% in ether-based electrolyte) and improved specific capacity in an ether-based electrolyte. Overall, the combination of flash pyrolysis and ether-based electrolyte increases the sodium-ion battery discharge capacity of coal char by over 50%, from 72.5 mAh g $^{-1}$ (slow-pyrolyzed char in ester-based electrolyte) to 109.4 mAh g $^{-1}$ (flash-pyrolyzed char in ether-based electrolyte) (50 mA g $^{-1}$ discharge rate). The results highlight improvements that can be realized through flash pyrolysis of coal char for battery applications and the numerous processing advantages of flash vs. slow pyrolysis.

1. Introduction

The past decade has seen a drastic emphasis on the need for the reduction of greenhouse gas emissions. One of the primary sources of worldwide CO₂ emissions is electric power generation through the combustion of fossil fuels [1]. Renewable technologies such as wind and solar power generation can greatly reduce greenhouse gas emissions; however, widespread replacement of baseload fossil-fuel electricity generation is challenging due to the intermittent availability of wind and solar power. For such a transition to be feasible, a major increase in electrical energy storage must be implemented in conjunction with wind and solar energy generation. Lithium-ion batteries (LIBs) have been the preferred electrochemical energy storage technology since the 1990s due to lithium's high theoretical specific capacity (3860 mAh g^{-1}) [2]. Concerns regarding the limited global availability and high production costs of lithium have prompted renewed research interest in alternative energy technologies, including sodium-ion batteries (SIBs) [3,4]. Sodium has a significantly lower cost of carbonate precursor (\$150 per metric ton of sodium carbonate) compared to lithium (\$13,000 per metric ton of lithium carbonate) [5]. Sodium is also one of the most abundant elements in the Earth's crust (2.36%) and has an estimated US abundance of 23 million tons [5]. The commercialization of SIBs is a major step towards domestic production of energy storage technologies within the continental US. In addition, SIBs provide a complimentary energy storage technology to LIBs, especially in stationary applications [6]. Sodium has a high theoretical specific capacity (1166 mAh g⁻¹) [7], but commercialization has been limited to-date due to challenges with economies of scale, low energy density, and poor cycling stability [8], as well as a lack of a true understanding of sodiation/desodiation mechanisms [9].

Graphite has been used as an industry standard LIB anode material, as graphite's extensive stacked nanosheets permit lithiation between graphene layers for ion storage. Graphite has shown difficulty being implemented into SIBs due to both the larger cation radius of Na $^+$ (1.06 Å) $vs.\ Li^+$ (0.76 Å) and the thermodynamic instability of sodium graphite intercalation compounds in ester-based electrolytes. Stevens and Dahn

E-mail address: jaron.moon@utah.edu (J.V. Moon).

^{*} Corresponding author.

first highlighted graphite intercalation issues where graphite anodes showed a low reversible sodium storage capacity of only $\sim\!\!35$ mAh g $^{-1}$ [10]. Hard carbons are an accepted replacement for graphite in SIBs due to their inhomogeneous internal structure characterized by short-order graphite microdomains within which sodium ions reversibly intercalate [9]. Doeff et al. first introduced the possibility of a full cell SIB design using a hard carbon petroleum coke anode [3]. Since then, many hard carbons have been investigated as potential SIB anode materials, including coal char.

Coal char has been explored as a hard carbon anode for SIBs due to its high availability, low cost, and high carbon content. While the abatement of coal-based power production is necessary for a net zero emission infrastructure, coal processing is still heavily desired as coal char can be an important source of rare earth elements [11]. Using coal char for SIB anodes provides a secondary, high-value application for coal that could be coupled with rare earth element extraction. To synthesize coal charderived hard carbon anodes, raw coal is heated in an inert atmosphere to remove moisture and volatiles, followed by high-temperature carbonization. Additional processing may also be implemented, such as acid washing [12], base washing [13], high concentration acid washing [14], or freeze drying [15]. Zheng et al. presented the use of coal for anodes in LIBs, showing that high-capacity hard carbon anodes consist of nanoscopic pores with small fractions of stacked graphene layers [16]. Lu et al. compared the use of different ranked coals in SIBs, demonstrating that electrochemical performance, initial Coulombic efficiency (ICE) and capacity retention are dependent on the degree of graphitization [17]. Kang et al. implemented an acid washing process for anthracite coal using HF, as well as ultrasonic stripping to create a coal charderived hard carbon anode with a high reversible capacity [14].

This work explores a novel technique for preparing SIB coal char anodes using flash pyrolysis. Flash pyrolysis uses a drop tube furnace to heat pulverized coal char at an exceedingly high rate (≥1000 °C/s). Flash pyrolysis creates a porous char with a high carbon conversion value [18]. Additional advantages of flash pyrolysis include: eliminating long ramp and heating times associated with slow pyrolysis [19]; the opportunity for continuous flow (vs. batch) processing; and higher rare earth element recovery rates due to smaller char particle size. To date, there have been no explorations of flash pyrolysis in SIB anode applications, either as a stand-alone method of hard carbon anode preparation or when coupled with additional post-processing steps (e.g., acid washing).

In this work, a bituminous, low sulfur coal is treated by flash pyrolysis (1000 °C/s) and compared with the same coal treated by slow pyrolysis (20 °C/min heating rate, 0.33 °C/s). Flash pyrolysis has yet to be studied for battery applications and introduces a new field of materials that may be viable for anode preparation. To isolate heating-rate effects on SIB anode performance, no further post-processing of the coal char is performed. Post-pyrolysis processing steps such as acid washing may certainly be coupled with flash pyrolysis in future studies. The effects of high vs. low heating rate on hard carbon material structure is investigated via scanning electron microscopy (SEM) imaging, highresolution transmission electron microscopy (HRTEM), thermogravimetric analysis (TGA), energy-dispersive X-ray spectroscopy (EDX), Xray diffraction (XRD), X-ray photoelectron spectroscopy (XPS), surface adsorption measurements (BET), and small-angle X-ray scattering (SAXS). SIB anode performance is quantified by direct comparison of flash-pyrolyzed (FP) char vs. slow-pyrolyzed (SP) char anodes in sodium half-cells. A further comparison is made regarding the SIB performance of FP char and SP char in ether- vs. ester-based electrolytes. Prior to this work, it has been shown that ether-based electrolytes, when implemented in SIBs, create a thinner, more conformal, solid electrolyte interphase (SEI) layer on hard carbon anodes than ester-based electrolytes, allowing for larger charge storage capacities as well as stable cycling [20-22]. Additionally, Kim et al. demonstrated that ether-based electrolytes promote the formation of sodium-graphite intercalation compounds, allowing for better plateau capacity [23]. In this work,

statistical analysis of first cycle discharge capacity, initial Coulombic efficiency (ICE) and tenth cycle discharge capacity is used to report statistically significant differences in the measured electrochemical results. The results demonstrate a statistically significant increase in the reversible capacity of FP-ether SIB half-cells compared to FP-ester, SP-ether, and SP-ester cells, with FP-ether half cells achieving a reversible capacity of 109.4 mAh g $^{-1}$ at C/2. The results show that FP char has superior performance as an anode material for SIBs compared to SP char It is expected that capacity results could be further improved in future studies by coupling flash pyrolysis with additional coal char processing steps.

2. Materials and Methods

2.1. Material Preparation

Raw, bituminous, coal was obtained from the Utah SUFCO mine, with particle size ranging from 75 μm to 125 μm . To prepare FP char, 5 g of SUFCO coal was loaded into a custom-built drop tube furnace (Fig. S1). Ultra-high purity nitrogen was used as both the carrier gas and the entrainment gas. The flow rate of the carrier gas was set at 4 L/min; the flow rate of the entrainment gas was set at 2 L/min. The carrier gas was preheated to 100 °C. The coal feeder tube gas flow rate was set at 0.5 L/min. Three heating zones, each measuring 0.3 m in length, were held at 900 °C, with a measured temperature difference of <15 °C between each zone. FP char was collected from the bottom of the drop tube furnace using $11 \mu m$ filter paper. When the drop tube furnace was loaded with 5 g of coal and run for 90 min, 3 g of coal was pyrolyzed and produced an average yield of 300 mg of char. This corresponds to a feed rate of 33.33 mg/min with a yield of 10%. SP coal char was prepared in a flatbed reactor with a heating rate of 20 °C/min in a nitrogen atmosphere. The char was heated to 900 $^{\circ}\text{C}$ and held at temperature for 20 min. The char was allowed to cool naturally to room temperature and collected.

FP and SP coal char samples were hand ground using a mortar and pestle, and sieved. Particles $<\!53~\mu m$ were collected and used for all further characterization and electrochemical testing. All char samples were stored under an inert atmosphere to prevent oxidation.

2.2. Material Characterization

TGA of coal char samples was completed at a heating rate of 5 °C/ min up to 950 °C on a TA Instruments Discovery SDT 650 using smart feature burn under nitrogen flow. SEM images and EDX measurements were obtained using a FEI Quanta 600 FEG. All reported EDX values are averaged across three different sample areas. HRTEM images were obtained using a JEOL JEM 2800 STEM. Char samples were dry-cast onto a TEM grid for imaging. Pore size distribution and specific surface area measurements were conducted on a Micromeritics 3Flex. Sample surface preparation was completed by leaving the samples under vacuum for 24 h at room temperature, followed by degassing at 350 °C under nitrogen flow for 3 h. Lastly, the samples were degassed under vacuum at 300 $^{\circ}\text{C}$ before surface adsorption measurements began. CO2 surface adsorption measurements were conducted in an ice bath at 0 °C. Specific surface area was calculated using the Brunauer-Emmett-Teller (BET) method, and a density function theory (DFT) analysis was conducted to determine pore size distribution and micropore volume using a non-local density functional theory (NLDFT) model for CO2. XPS results were taken on a Kratos Axis Ultra with a monochromatic Al Ka source. A survey scan was first taken to determine which elements were present in the material, and high-resolution scans were taken for the reported elemental analysis. XRD data was collected using a Philips PANalytical X'Pert scanned from 0 to 80 degrees. SAXS analysis was completed using an Anton Paar SAXS 2.0 with Cu Ka radiation at detector distances of 250 mm and 80 mm. Char powders were loaded into a square analysis area between two pieces of Kapton tape with a thickness of 0.97 mm. A

vacant square with two pieces of Kapton tape was used for a background measurement. Transmittance values were taken for both areas to subtract the background noise from the char analysis.

2.3. Electrochemical Measurements

All materials were purchased from Millipore Sigma and used as received. Two electrolytes were used for electrochemical testing: an ether-based electrolyte and an ester-based electrolyte. The ether-based electrolyte was prepared by dissolving 1 M NaBF $_4$ in triethylene glycol dimethyl ether (TEGDME). The ester-based electrolyte was prepared by dissolving 1 M NaClO $_4$ in ethylene carbonate (EC) and tetrahydrofuran (THF) (1:1 by volume). Electrode slurry compositions were prepared using an 8:1:1 weight ratio of char, Super P, and polyacrylic acid (PAA) using N-methyl-2-pyrrolidone (NMP) as the suspension solution. The prepared slurry was coated on copper current collector disks with a diameter of 15 mm. Active material loading was constrained to 1.5–2.0 mg/cm 2 . After coating, char anodes were dried at 80 °C for 24 h under vacuum.

Coin cells were fabricated in a LC Technology LCPW-1 glovebox with argon atmosphere where oxygen and water levels were <0.1 ppm. CR2023 cells were fabricated using a sodium disc as the cathode, two 2340 Celgard separators, and a FP or SP char anode. The coin cells were pressed using an MTI MSK-160E electric crimper.

All coin cells were allowed to rest 24 h prior to testing to confirm sealing and stability, followed by checking of the open circuit potentials for 1 h. Constant current charge-discharge tests of prepared coin cells were completed on a Battery Metric Battery Analyzer. Cyclic voltammetry (CV), electrochemical impedance spectroscopy (EIS), cycle life, and rate capability tests of coin cells were completed using a Gamry Interface 1000E Potentiostat. EIS measurements were performed at 0% state-of-charge. Plateau capacity was determined to be when the discharge voltage was $\leq\!0.1$ V; sloping capacity was considered to be when the discharge voltage was $>\!0.1$ V.

2.4. Statistical Analysis

A statistical analysis was conducted using a single factor ANOVA to determine a significant difference among all char-electrolyte configurations. An independent, two-tail t-test was completed to compare individual differences between each char-electrolyte configuration. A p-value <0.05 was used to denote significance. A count number of at least three cells was used for each char-electrolyte configuration.

3. Results and Discussion

3.1. Slow- vs. Flash-Pyrolyzed Char Characterization

Flash pyrolysis produces rapid heating by exposing highly dispersed, small (typically $<\!200~\mu m$) coal particles to the environment within the drop tube furnace. The heating rate for the drop tube furnace used in this study was estimated using the equations and approach presented by Rußig et al. [24], as described in the SI. Heating rate and residence time are a function of: particle size and density; carrier gas velocity, density and dynamic viscosity; and furnace temperature. Particle size and density affect gravity-induced sedimentation velocity. The high surface-to-volume ratio of the micron-sized coal particles results in a rapid heat flux through the particles, quickly increasing particle temperature. The estimated residence time of feed particles across all three heating zones is 0.837 s (Fig. S2). This corresponds to an estimated heating rate of 1075.1 °C/s (reported as 1000 °C/s throughout the manuscript), and a maximum temperature of 900 °C. The calculated results are similar to other heating rates reported in literature for drop tube furnaces [25–27].

SEM images of FP and SP char (Fig. 1) reveal major differences in char particle morphology due to the different heating rates. SP char exhibits a flat, uniform, solid surface structure with jagged edges (Fig. 1d,e). FP char presents a vastly different particle morphology with large surface distortions, nonuniform edges, and irregular surface features (Fig. 1a,b). The irregular structure of FP char is created as volatiles and water vapor are released from the coal at a high velocity due to the intense heating rate. The flash pyrolysis parameters used in this study produce a significant amount of soot along with the coal char. Soot is

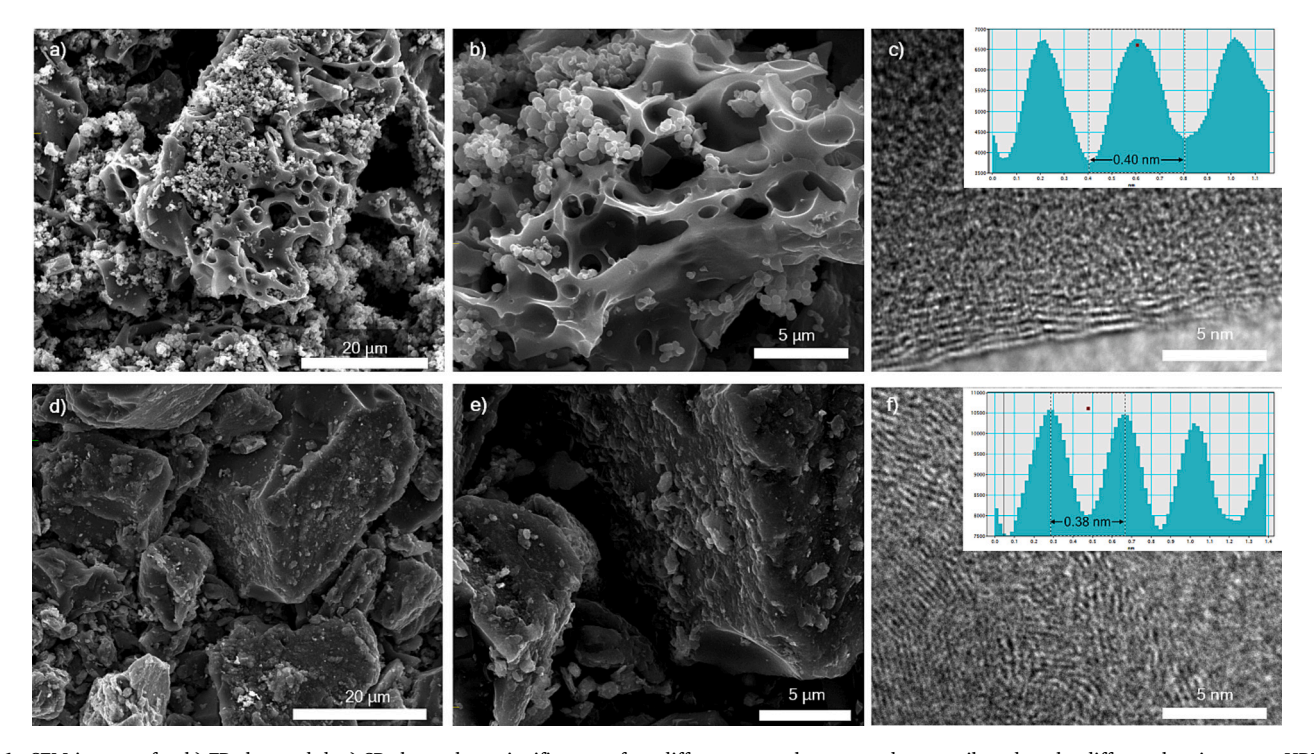


Fig. 1. SEM images of a, b) FP char and d, e) SP char, where significant surface differences can be seen and are attributed to the different heating rates. HRTEM images of c) FP char, and f) SP char, with measured lattice spacing measurements shown inset in each fig.

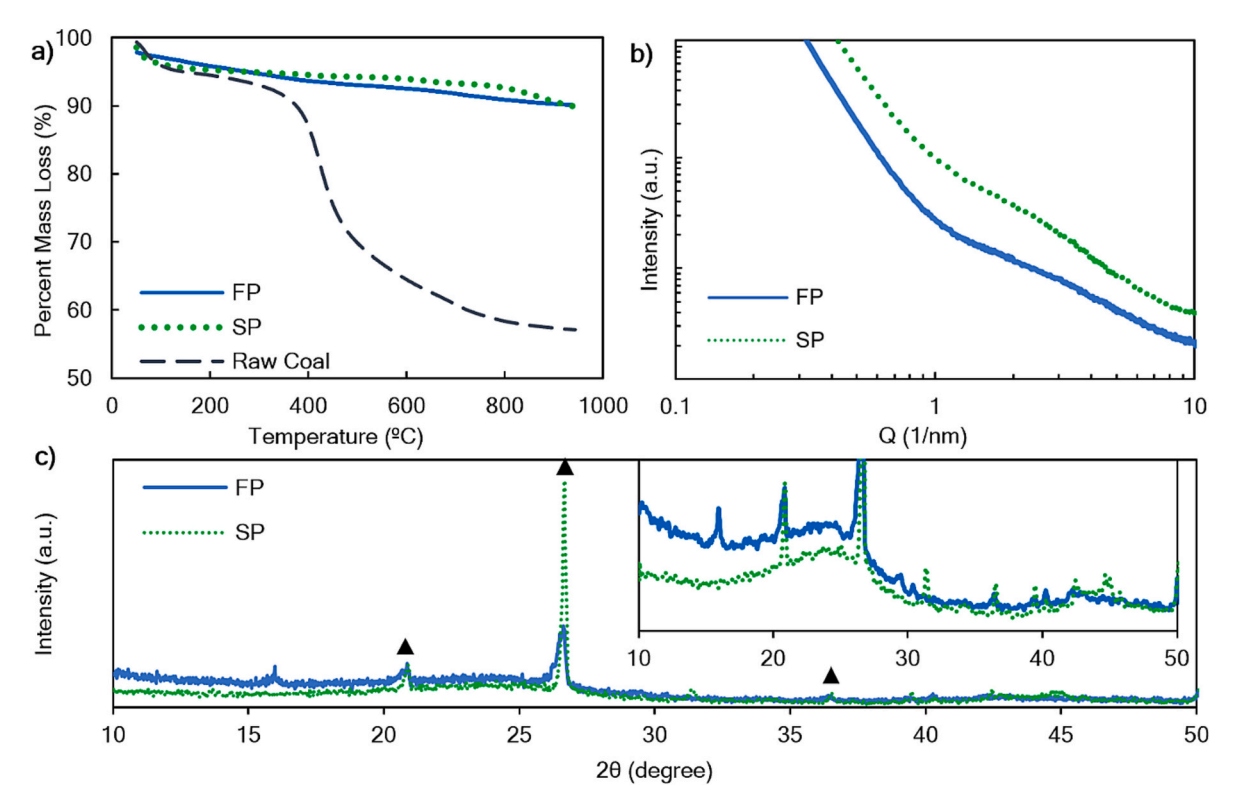


Fig. 2. Material property characterization of FP and SP char. a) TGA comparison of FP char, SP char, and raw coal. b) SAXS curves of FP and SP char. c) XRD spectra of FP and SP char from 10 to 50 degrees (2θ). Black triangles indicate impurity peaks from SiO₂.

formed at high heating rates due to secondary reactions in which volatiles, often coal tar, are released into the gas phase and undergo further reactions and then condense on the char surface [28]. The effect of soot on the SIB performance of FP char is explored briefly in the SI (Fig. S3-S4, Table S1). SP char does not contain visible quantities of soot.

Fig. 1c and Fig. 1f provide HRTEM images of FP and SP char, respectively. HRTEM images were taken at the fringe edges of the dry-cast particles to view individual lattices. Differences in lattice spacing between the two chars are clearly visible in the high-resolution images and in the lattice spacing measurement plots. FP char has a larger measured d-spacing of 0.40 nm, whereas SP char measures 0.38 nm (Fig. 1c,f). Further analysis of d-spacing through XRD and SAXS is provided below. Low magnification TEM images of FP and SP char are provided in Supporting Information Fig. S5. The images suggest distinct differences in elemental composition of the two chars. SP char shows dark regions within the particle (Fig. S5a), denoting transition metal impurities located inside the particles. FP char does not show these same heavy metal impurities (Fig. S5b).

FP vs. SP char composition is compared to SUFCO raw coal through TGA,EDX, and XPS measurements. TGA results for raw coal show a high mass loss from 90% (after initial moisture loss) to 70% at $\sim\!450~^{\circ}\text{C}$, followed by a slow mass loss to 58% by 950 $^{\circ}\text{C}$ (Fig. 2a). In contrast, FP and SP char samples only lose $\sim\!8\%$ mass after heating to 950 $^{\circ}\text{C}$. FP and SP char samples have similar mass loss characteristic curves, indicating that both heating methods result in equally pyrolyzed char.

Table 1 compares EDX and XPS elemental analysis of the char samples. EDX results indicate that FP char has a high carbon content (83 wt %) compared to SP char (75 wt%) and raw coal (76 wt%). The higher carbon content and lower oxygen content of FP char vs. SP char is further confirmed using XPS (95 wt% C, 3 wt% O for FP char vs. 73 wt% C, 15 wt % O for SP char). Differences in wt% values measured by EDX vs. XPS are attributed to differences in measurement depth. XPS is a surface-sensitive measurement (~ 10 nm depth), whereas EDX can measure up to a few micrometers below the sample surface. XPS survey scan

Table 1 EDX and XPS elemental composition results for raw coal, FP char, and SP char.

	Raw Coal (wt%)	FP Char (wt%)		SP Char (wt%)	
	EDX	EDX	XPS	EDX	XPS
С	76	83	95	75	73
O	20	12	3	12 3	15 4
Si	1	3	0.4		
Ca	0.5	0.5	0	3	4
All other	2.5	1.5	1.6	6	4

results of SP char and FP char are provided in the SI (Fig. S6), where the carbon-to-oxygen peak intensity ratios are considerably different between FP and SP char. XPS and EDX results in combination show the carbon retention improvements of flash pyrolysis compared to slow pyrolysis.

The internal structure of FP vs. SP char, including open vs. closed pore size and density, will affect the char's SIB anode performance [13]. CO2 adsorption measurements of FP and SP char indicate comparable microporous surface area and micropore structure for the two chars. SP char shows a slightly larger specific surface area (169.73 m²/g) than FP char (161.03 m 2 /g). DFT pore size analysis using a NLDFT model for CO $_2$ indicates a SP char micropore volume of $0.039~\text{cm}^3/\text{g}$ for pores less than or equal to 4.45 Å, whereas FP char has a micropore volume of 0.035 cm³/g for pores less than or equal to 4.45 Å. Combining these results with insights from SEM images, it is clear that FP char has larger macropores but comparable micro- and mesopores (< 50 nm) as SP char. CO₂ adsorption/desorption was chosen due to the undesirable surface kinetics of nitrogen on coal samples [29], and because CO₂ can infiltrate smaller pores at a higher temperature, due to its smaller kinetic diameter [30]. Pore size distribution and adsorption/desorption curves are provided in the SI (Fig. S7).

SAXS analysis was completed on FP and SP char (Fig. 2b) to elucidate changes in internal pore structure that occur as a result of rapid heating. SAXS intensity curves with their respective fits are provided in Fig. S8,

Table 2 d-spacing and micropore diameter of FP and SP char, as determined from XRD/HRTEM and SAXS, respectively.

	d-spacing [nm] (XRD)	d-spacing [nm] (HRTEM)	d _{micropore} [nm] (SAXS)
FP char	0.379	0.40	1.52
SP char	0.364	0.38	1.91

with calculated fitting variables provided in Table S2. Internal closed pore diameters are calculated as described in the SI. From the fitted curves, the calculated internal closed-pore diameter of FP char is 1.52 nm, compared to 1.91 nm for SP char. The larger internal closed pore diameter of SP char is attributed to the slow heating rate promoting gradual transitions of graphene internal structure during pyrolysis. Gradual transitions allow the graphene sheet interspatial distance to decrease, thereby creating larger closed pores. FP char is heated so rapidly that no restructuring is allowed, producing an internal structure with smaller closed pores.

The internal structure of FP vs. SP char was further analyzed using XRD. A d-spacing of 0.37 nm is reported as the ideal spacing for sodiation/desodiation during charge/discharge cycling of SIB hard carbon anodes [31]. XRD measurements of FP and SP char (Fig. 2c) indicate that the chars are mixtures of amorphous carbon and crystalline impurities. FP char has a d-spacing of 0.379 nm, compared to 0.364 nm for SP char (Table 2), as calculated from the (002) broad peak location. Both FP and SP char samples display broad peaks centered around \sim 24 and \sim 45 degrees [32], representing the (002) and the (100) planes of amorphous hard carbon, respectively. Sharp peaks present in the XRD spectra of FP and SP char are attributed to crystalline impurities in the char. The most prominent impurity is SiO2, which is consistent with previous studies of coal char composition [17]. XRD d-spacing measurements of SP and FP char are consistent with HRTEM results, as summarized in Table 2. The differences in the lattice spacing results from the XRD to HRTEM values can be understood in the XRD amorphous peak, indicating many dspacing values are present in the char, making it difficult to determine an exact value, yet qualitatively, from both XRD and HRTEM measurements, it can be concluded that FP char has a larger d-spacing value.

3.2. Electrochemical results

Electrochemical characterization was completed on half cells assembled with a sodium metal cathode and coal char anode. Four types of cells were assembled: 1) FP char in ether-based electrolyte, 2) FP char in ester-based electrolyte, 3) SP char in ether-based electrolyte, and 4) SP char in ester-based electrolyte. The anion BF $_4^-$ was used with the ether-based electrolyte due to its reported superior performance when paired with ether electrolytes [33]. The anion ClO $_4^-$ was used with the ester-based electrolyte due to its widespread utilization in SIB literature [22,34]. Electrochemical testing was completed to explore the storing mechanism of FP char and evaluate the effectiveness of ether- ν s. ester-based electrolytes with coal char anodes.

EIS was completed on all four cells, with Fig. 3 providing Nyquist plots for each cell. The EIS characteristics of each cell can be described with the equivalent circuit shown in Fig. 3, using best-fit parameters provided in Table 3. The equivalent circuit consists of a series resistance (R_S), a charge transfer resistance (R_{CT}), and two constant phase elements: 1) CPE_W and associated α_W (in place of the frequently used Warburg element), and 2) a charge transfer resistance element (CPE_{CT} and associated α_{CT}). Ether cells show a minimal semicircular region at low impedance, followed by a long tail indicative of diffusion impedance of sodium ions into the bulk char [35]. Ester cells, in contrast, show a large semicircular region indicative of a larger charge transfer resistance (R_{CT} = 200 Ω for FP-ester compared to R_{CT} = 33 Ω for FP-ether). The

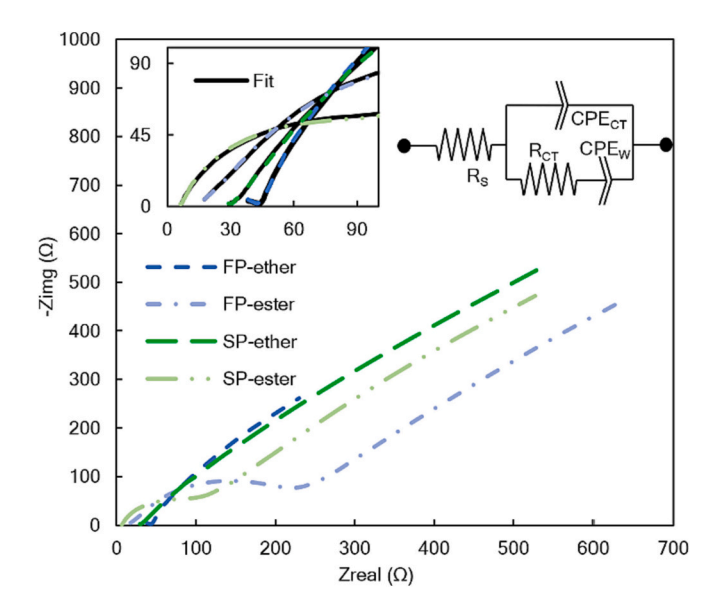


Fig. 3. Nyquist plots of EIS measurements for FP-ether, FP-ester, SP-ether, and SP-ester cells. Inset shows high frequency EIS results (with fit) and equivalent circuit used for modeling.

diffusion coefficient of sodium ions in each configuration is calculated as described in [36] (Table 3). As anticipated, the FP-ether cell has the highest ion diffusion coefficient $(1.25*10^{-11}~\text{cm}^2/\text{s})$. This measured value matches well with other literature values [37], and further indicates the improvements of an ether electrolyte.

FP-ether cell performance is compared to other cell configurations through constant current cell cycling. Table 4 provides electrochemical performance values, including ICE, first cycle discharge capacity, and tenth cycle discharge capacity, for all cell configurations. FP-ether cells have the highest ICE (64%), followed by FP-ester (58%). SP-ether and SP-ester cells have comparable ICE values (52%). Most frequently, it is reported that ICE values directly relate to the formation of the SEI [38]. Higher ICE values for SIB hard carbon anodes are typically reported with ether-based electrolytes vs. ester-based electrolytes due to the formation of a thinner, more conformal SEI [39]. It has been shown that SEI growth can occur within closed micropores, which may explain the lower ICE values for SP char [40]. The fact that FP char attains larger ICE values than SP char for both electrolytes suggests that rapid heating creates a better char composition in regard to SEI formation. Discharge capacities of FP-ether cells are higher than all other cell configurations with first and tenth cycle capacities measuring 173.4 mAh g⁻¹ and 109.4 mAh g⁻¹, respectively. Transitioning from a SP-ester cell to a FP-ester cell increases specific capacity by 30%. A 51% specific capacity increase is realized when a FP-ether cell is compared to a SP-ester cell.

Capacity improvements achieved with flash pyrolysis and etherbased electrolyte can be explained by closer examination of discharge curve sloping *vs.* plateau regions. An adsorption-insertion-nanopore filling model is commonly used to understand sodium ion storage

Table 3EIS equivalent circuit value model parameters.

	FP-ether	FP-ester	SP-ether	SP-ester
$R_s(\Omega)$	20	16	15	6
$R_{CT}(\Omega)$	45.0	368.1	40.0	142.7
CPE_{CT} (10 ⁻⁴ Ss^{α})	8.40	0.58	2.40	0.99
α_{CT}	0.26	0.78	0.45	0.85
$CPE_W (10^{-4} Ss^{\alpha})$	1.10	1.89	0.44	1.23
α_{W}	0.86	0.77	0.68	0.86
Goodness of Fit (10^{-3})	0.9	2.4	8.6	4.6
Na ⁺ Diffusion Coefficient (cm ² /s)	$1.25*10^{-11}$	$1.00*10^{-12}$	$8.22*10^{-13}$	$9.72*10^{-13}$

Table 4 Electrochemical performance summary of the four cell configurations.

Cell	1st Cycle Discharge Capacity [mAh ${\sf g}^{-1}$]	10th Cycle Discharge Capacity [mAh ${\rm g}^{-1}$]	ICE	1st Cycle Plateau Percentage	10th Cycle Plateau Percentage
FP-	173.4	109.4	64%	16%	18%
ether					
FP-ester	165.4	95.4	58%	14%	14%
SP-	136.3	84.0	52%	24%	31%
ether					
SP-ester	131.5	72.5	52%	14%	21%

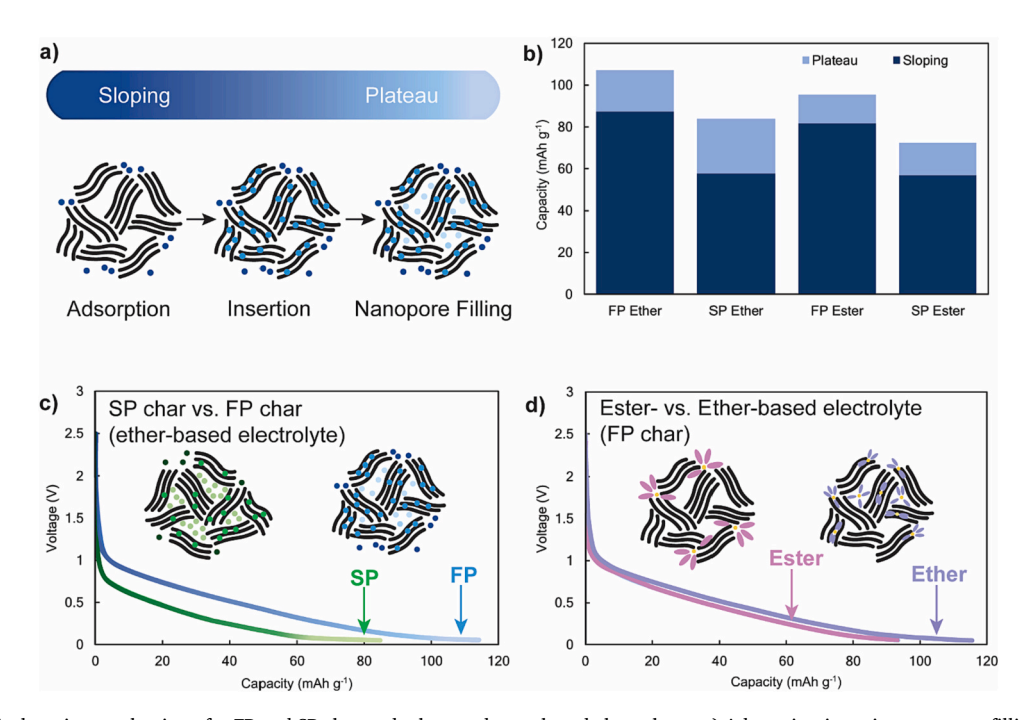


Fig. 4. Electrochemical storing mechanisms for FP and SP char and ether- and ester-based electrolytes. a) Adsorption-insertion-nanopore filling model shown in the hard carbon domain. b) Tenth cycle discharge curves denoting specific capacity for the sloping and plateau regions. c) Tenth cycle discharge curves of FP-ether and SP-ether cell to convey the FP vs. SP char storing mechanism. d) Tenth cycle discharge curves of FP-ether and FP-ester cells to convey ether- vs. ester-based electrolyte ion insertion of solvated ions.

mechanisms and discharge curve characteristics in hard carbon anodes [41]. In this model, initial sloping capacity is attributed to capacitive charge storage *via* sodium ion adsorption on active sites (*e.g.*, defects, heteroatoms) [42]. The remaining sloping-plateau region is attributed to insertion of ions in graphite sheets, followed by nanopore filling

(Fig. 4a).

Fig. 4b plots sloping vs. plateau capacities of tenth cycle discharge results for all four cell configurations. FP char shows larger sloping capacity values which can be attributed to greater capacitive storage of sodium ions compared to SP char (Fig. 4b, c) [37]. Increased presence of

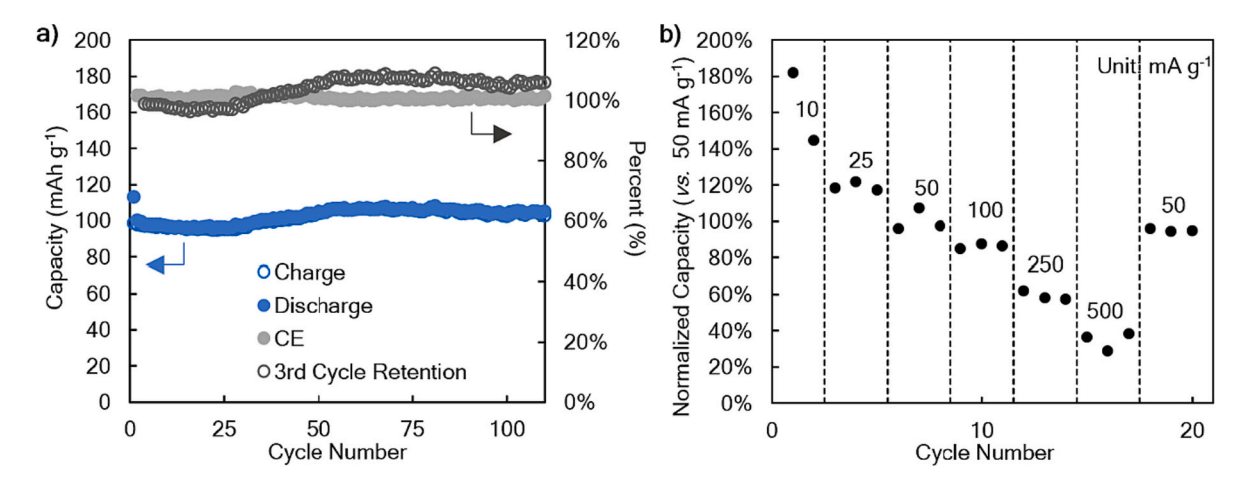


Fig. 5. a) Cycle performance of FP-ether cells, including charge capacity (mAh g⁻¹), discharge capacity (mAh g⁻¹), CE, and third cycle capacity retention. b) Rate capability of FP-ether cells.

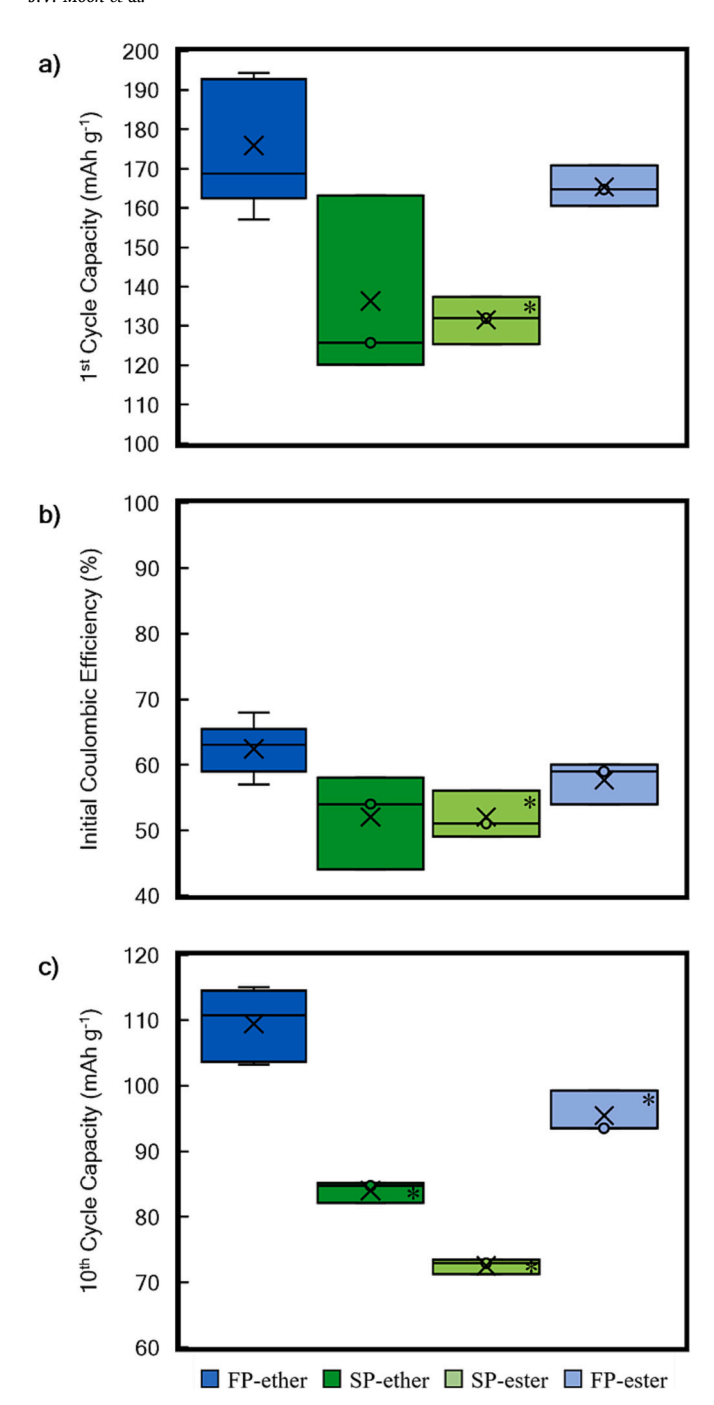


Fig. 6. Box and whisker plots for a) first cycle discharge capacity, b) ICE, c) and tenth cycle discharge capacity for FP-ether, SP-ether, SP-ester, and FP-ester cell configurations. An * denotes results are significantly different than the FP-ether cell result

defect sites promoting sodium ion adsorption is consistent with the rapid heating mechanism of flash pyrolysis. SP char shows larger plateau percentages compared to FP char. SP char has a larger internal closed pore diameter, which has been shown to increase nanopore filling. Higher capacitive storage in FP char and increased nanopore filling in SP char are consistent with CV measurements, as reported in the Supporting Information (Fig. S9).

The switch from an ester- to an ether-based electrolyte increases plateau capacity percentages for both FP and SP char electrodes (Table 4). Plateau capacity in hard carbon anodes is attributed to both nanopore filling and insertion between graphite sheets [23,43]. In this

case, plateau capacity increase is attributed to the ether-based electrolyte enabling the formation of graphite intercalation compounds in both FP and SP char electrodes where solvated ions in an ether electrolyte promote better storing of sodium ions (Fig. 4b, d).

Cycle life and rate capability were further explored for FP-ether cells, as shown in Fig. 5. SIB half cells constructed using FP char show stable cycling and good rate capability. Hard carbon anodes for SIBs often suffer from poor rate capability and unstable cycling. This has been attributed to unstable SEI layers increasing charge transfer resistance and creating large voltage hysteresis [44]. Over 100 cycles, FP-ether cells achieve a capacity retention over 100% of their third cycle discharge capacity (Fig. 5a). A Coulombic efficiency (CE) of 100% is achieved on the second cycle and maintained over 100 cycles. The high CE of FP-ether cells is attributed to the ether-based electrolyte allowing for efficient ion transfer, resulting in effective capacity retention [45]. FP-ether cells also show good rate capability, retaining 34% capacity when the C-rate increases from C/2 (50 mA g $^{-1}$) to 10C (500 mA g $^{-1}$). 95% capacity recovery is achieved when the discharge rate returns to 50 mA g $^{-1}$ from 500 mA g $^{-1}$ (Fig. 5b). [40]

3.3. Statistical Analysis

To determine statistical significance of the reported half-cell results, box and whisker plots were created for first cycle discharge capacity (Fig. 6a), ICE (Fig. 6b), and tenth cycle discharge capacity (Fig. 6c). A single-factor ANOVA of first cycle discharge capacity indicates that the results among cell configurations are significant (F_{3,10} = 7.621, p = 0.005). When using a t-test to determine significance, first cycle discharge capacity differences are abstruse. FP-ether first cycle discharge capacity values are significantly different from SP-ester results (M_{FP-ether} = 173.4 mAh g⁻¹, M_{SP-ester} = 136.3 mAh g⁻¹, t(5) = 5.53, p = 0.003). FP-ether and SP-ether first cycle discharge capacity show no significant difference (M_{FP-ether} = 173.4 mAh g⁻¹, M_{SP-ether} = 136.3 mAh g⁻¹, t(5) = 2.57, p = 0.082).

ICE and tenth cycle capacity ANOVA results show significant differences among the cell configurations (F_{3,10} = 4.63, p = 0.028) and (F_{3,10} = 62.75, p < 0.001), respectively. For ICE, a t-test indicates the only significant difference is between FP-ether and SP-ester (M_{FP-ether} = 64%, M_{SP-ester} = 52%, t(5) = 3.8, p = 0.082). Paired comparisons of tenth cycle discharge values by t-test indicate significant differences between all combinations of electrolyte and char. Ether-based cells have significantly greater tenth cycle capacity than ester-base cells for both chars (FP: M_{FP-ether} = 109.4 mA g⁻¹, M_{FP-ester} = 95.4 mA g⁻¹, t(6) = 4.46, p < 0.05).

4. Conclusion

SIB technology using coal-derived anodes represents a low-cost approach for energy storage applications that use more abundant natural resources than conventional LIB technology. This work presents a novel approach using rapid heating via flash pyrolysis (1000 °C/s) to create hard carbon anodes from a bituminous coal for SIBs that improves anode capacity relative to conventional slow pyrolysis approaches. The SIB performance of FP and SP chars were compared in two different electrolytes: 1) an ether-based electrolyte, NaBF4 in TEGDME, and 2) an ester-based electrolyte, NaClO₄ in EC:THF. FP char in ether-based electrolyte outperformed all other cell configurations due to the positive impacts of flash pyrolysis combined with the positive attributes of an ether-based electrolyte for SIB design. Flash pyrolysis creates a char with highly irregular surface morphology, a larger d-spacing, and smaller internal pore diameter, compared to SP char. These structural differences create a discharge curve that has a larger sloping region, while also increasing ICE. FP-ether cells achieve a reversible capacity of 109.4 mAh g^{-1} and 64% ICE, compared to 72.5 mAh g^{-1} and 52% ICE for SP-ester cells, which is a 51% specific capacity improvement. Due to its numerous processing advantages, it is recommended that flash

pyrolysis be explored in conjunction with other hard carbon processing techniques for coal char-based SIB anodes, such as acid washing or other deashing techniques, to further advance the potential for coal char as a hard carbon anode for SIBs.

Declaration of Competing Interest

The authors declare that they have no known competing financial interests or personal relationships that could have appeared to influence the work reported in this paper.

Data availability

All data supporting this work can be made available upon request to the corresponding author.

Acknowledgments

The authors would like to thank the University of Utah Electron Microscopy and Surface Analysis Lab Scientist's for their helpful guidance and training that made this work possible.

Funding

This work was supported in-part by NSF Award #2152562 and the University of Utah Department of Mechanical Engineering. This work made use of University of Utah USTAR shared facilities supported, in part by the MRSEC Program of the NSF under Award No. DMR-1121252.

Author contributions

Jaron V. Moon – Data curation, Formal Analysis, Investigation, Project Administration, Supervision Writing - original draft, review, and editing.

Zahra Karimi – Investigation.

Alex Prlina - Resources, Software.

Chanel van Ginkel - Investigation.

Danielle M. Horlacher - Visualization.

 $\operatorname{Eric} G.$ Eddings – Conceptualization, Resources, Writing – review and editing.

Roseanne Warren – Conceptualization, Funding Acquisition, Supervision, Writing – review and editing.

Appendix A. Supplementary data

Supplementary data to this article can be found online at https://doi.org/10.1016/j.fuproc.2023.107998.

References

- M.J.B. Kabeyi, O.A. Olanrewaju, Sustainable energy transition for renewable and low carbon grid electricity generation and supply, Front Energy Res 9 (2022), 743114, https://doi.org/10.3389/fenrg.2021.743114.
- [2] B. Liu, J.G. Zhang, W. Xu, Advancing Lithium Metal Batteries, Joule 2 (2018) 833–845. https://doi.org/10.1016/j.joule.2018.03.008.
- [3] M.M. Doeff, Y. Ma, S.J. Visco, L.C. De Jonghe, Electrochemical Insertion of Sodium into Carbon, J. Electrochem. Soc. 140 (1993) L169–L170, https://doi.org/ 10.1140/1.2221153
- [4] Z. Lou, H. Wang, D. Wu, F. Sun, J. Gao, X. Lai, Microcrystalline regulation of bituminous coal derived hard carbon by pre-oxidation strategy for improved sodium-ion storage, Fuel 310, no. PB (2022), 122072, https://doi.org/10.1016/j fuel.2021.122072.
- [5] H.S. Hirsh, Y. Li, D.H.S. Tan, M. Zhang, E. Zhao, Y.S. Meng, Sodium-Ion Batteries Paving the way for Grid Energy Storage, Adv. Energy Mater. 10 (2020) 2001274, https://doi.org/10.1002/aenm.202001274.
- [6] K.M. Abraham, How comparable are Sodium-Ion Batteries to Lithium-Ion Counterparts? ACS Energy Lett. 5 (2020) 3544–3547, https://doi.org/10.1021/ acsenergylett.0c02181.
- [7] B. Sun, et al., Design strategies to Enable the Efficient use of Sodium Metal Anodes in High-Energy Batteries, Adv. Mater. 32 (2020) 1903891, https://doi.org/ 10.1002/adma.201903891.

- [8] K. Chayambuka, G. Mulder, D.L. Danilov, P.H.L. Notten, From Li-Ion Batteries toward Na-Ion Chemistries: challenges and Opportunities, Adv. Energy Mater. (2020) 2001310, https://doi.org/10.1002/aenm.202001310.
- [9] D. Chen, et al., Hard carbon for sodium storage: mechanism and optimization strategies toward commercialization, Energy Environ. Sci. 14 (2021) 2244–2262, https://doi.org/10.1039/d0ee03916k.
- [10] D.A. Stevens, J.R. Dahn, The Mechanisms of Lithium and Sodium Insertion in Carbon Materials, J. Electrochem. Soc. 148 (2001) A803, https://doi.org/10.1149/ 1.1379565.
- [11] S. Park, et al., Characterization of rare earth elements present in coal ash by sequential extraction, J. Hazard. Mater. 402 (2021), 123760, https://doi.org/ 10.1016/j.jhazmat.2020.123760.
- [12] J. Li, et al., Constructing graphene-like nanosheets on porous carbon framework for promoted rate performance of Li-ion and Na-ion storage, Electrochim. Acta 271 (2018) 92–102, https://doi.org/10.1016/j.electacta.2018.02.147.
- [13] K. Wang, et al., Altering thermal Transformation Pathway to create Closed Pores in Coal-Derived Hard Carbon and Boosting of Na+ Plateau Storage for High-Performance Sodium-Ion Battery and Sodium-Ion Capacitor, Adv. Funct. Mater. 32 (2022) 2203725, https://doi.org/10.1002/adfm.202203725.
- [14] M. Kang, et al., Adsorption dominant sodium storage in three-dimensional coal-based graphite microcrystal/graphene composites, J Mater Chem A Mater 7 (2019) 7565–7572, https://doi.org/10.1039/C8TA12062E.
- [15] S. Gao, et al., Coal-based Hierarchical Porous Carbon Synthesized with a Soluble Salt Self-Assembly-Assisted Method for High Performance Supercapacitors and Li-Ion Batteries, ACS Sustain. Chem. Eng. 6 (2018) 3255–3263, https://doi.org/ 10.1021/acssuschemeng.7b03421.
- [16] T. Zheng, W. Xing, J.R. Dahn, Carbons prepared from Coals for Anodes of Lithiumion Cells, Carbon N Y 34 (12) (1996) 1501–1507, https://doi.org/10.1016/S0008-6223(96)0098.X
- [17] H. Lu, et al., High-capacity Hard Carbon Pyrolyzed from Subbituminous Coal as Anode for Sodium-Ion Batteries, ACS Appl Energy Mater 2 (2019) 729–735, https://doi.org/10.1021/acsaem.8b01784.
- [18] K. Matsuoka, H. Akiho, W. Xu, R. Gupta, The physical character of coal char formed during rapid pyrolysis at high pressure, Fuel 84 (2005) 63–69, https://doi. org/10.1016/j.fuel.2004.07.006.
- [19] B. Xing, et al., Preparation of synthetic graphite from bituminous coal as anode materials for high performance lithium-ion batteries, Fuel Process. Technol. 172 (2018) 162–171. https://doi.org/10.1016/j.fuproc.2017.12.018.
- [20] H.S. Hirsh, et al., Role of electrolyte in stabilizing hard carbon as an anode for rechargeable sodium-ion batteries with long cycle life, Energy Storage Mater 42 (2021) 78–87, https://doi.org/10.1016/j.ensm.2021.07.021.
- [21] P.K. Dutta, S. Mitra, Efficient sodium storage: Experimental study of anode with additive-free ether-based electrolyte system, J. Power Sources 349 (2017) 152–162, https://doi.org/10.1016/j.jpowsour.2017.03.031.
- [22] Z. Lin, Q. Xia, W. Wang, W. Li, S. Chou, Recent research progresses in ether- and ester-based electrolytes for sodium-ion batteries, InfoMat 1 (2019) 376–389, https://doi.org/10.1002/inf2.12023.
- [23] H. Kim, J. Hong, Y.U. Park, J. Kim, I. Hwang, K. Kang, Sodium Storage Behavior in Natural Graphite using Ether-based Electrolyte Systems, Adv. Funct. Mater. 25 (2015) 534–541, https://doi.org/10.1002/adfm.201402984.
- [24] S. Rußig, V. Gonzalez, M. Schurz, J. Kleeberg, S. Guhl, B. Meyer, Particle residence time measurement in a pressurized drop-tube reactor with radioactive tracer, Fuel 252 (2019) 37–46, https://doi.org/10.1016/j.fuel.2019.03.134.
- [25] Z. Zhu, C. Zhang, X. Wang, The effect of volatile residence time on flash hydropyrolysis of Zalannoer lignite, Fuel Process. Technol. 15 (1997) 157–164, https://doi.org/10.1016/S0378-3820(97)00001-5.
- [26] W.C. Xu, K. Matsuoka, H. Akiho, M. Kumagai, A. Tomita, High pressure hydropyrolysis of coals by using a continuous free-fall reactor, Fuel 82 (2003) 677–685, https://doi.org/10.1016/S0016-2361(02)00340-X.
- [27] S. Heuer, et al., Effects of oxy-fuel conditions on the products of pyrolysis in a drop tube reactor, Fuel Process. Technol. 150 (2016) 41–49, https://doi.org/10.1016/j. fuproc.2016.04.034.
- [28] J. Ma, T.H. Fletcher, B.W. Webb, Conversion of coal tar to soot during coal pyrolysis in a post-flame environment, in: Symposium (International) on Combustion, 1996, pp. 3161–3167, https://doi.org/10.1016/S0082-0784(96) 80161-5.
- [29] Z. Karimi, J. Moon, J. Malzahn, E. Eddings, R. Warren, Ultra-low cost supercapacitors from coal char: effect of electrolyte on double layer capacitance, Energy Advances (2023), https://doi.org/10.1039/d3ya00064h.
- [30] S. Tan, T. John, K.D. Li-oakey, Understanding the supercapacitor properties of electrospun carbon nano fibers from Powder River Basin coal, Fuel 245 (2019) 148–159, https://doi.org/10.1016/j.fuel.2019.01.141.
- [31] Y. Cao, et al., Sodium ion insertion in hollow carbon nanowires for battery applications, Nano Lett. 12 (2012) 3783–3787, https://doi.org/10.1021/ nl3016957.
- [32] Z. Li, et al., Mechanism of Na-Ion Storage in Hard Carbon Anodes Revealed by Heteroatom Doping, Adv. Energy Mater. 7 (2017) 1602894, https://doi.org/ 10.1002/aenm.201602894.
- [33] K. Du, et al., A comprehensive study on the electrolyte, anode and cathode for developing commercial type non-flammable sodium-ion battery, Energy Storage Mater 29 (2020) 287–299, https://doi.org/10.1016/j.ensm.2020.04.021.
- [34] K. Kubota, S. Komaba, Review—Practical Issues and Future Perspective for Na-Ion Batteries, J. Electrochem. Soc. 162 (14) (2015) A2538–A2550, https://doi.org/ 10.1149/2.0151514jes.

- [35] B.A. Mei, O. Munteshari, J. Lau, B. Dunn, L. Pilon, Physical Interpretations of Nyquist Plots for EDLC Electrodes and Devices, J. Phys. Chem. C 122 (2018) 194–206, https://doi.org/10.1021/acs.jpcc.7b10582.
- [36] N. Ingersoll, Z. Karimi, D. Patel, R. Underwood, R. Warren, Metal organic framework-derived carbon structures for sodium-ion battery anodes, Electrochim. Acta 297 (2019) 129–136, https://doi.org/10.1016/j.electacta.2018.11.140.
- [37] D. Ledwoch, et al., Determining the electrochemical transport parameters of sodium-ions in hard carbon composite electrodes, Electrochim. Acta 401 (2022), 139481, https://doi.org/10.1016/j.electacta.2021.139481.
- [38] X. Li, et al., Review on comprehending and enhancing the initial Coulombic efficiency of anode materials in lithium-ion / sodium-ion batteries, Nano Energy 77 (2020), 105143, https://doi.org/10.1016/j.nanoen.2020.105143.
- [39] D. Saurel, B. Orayech, B. Xiao, D. Carriazo, X. Li, T. Rojo, From charge Storage Mechanism to Performance: a Roadmap toward High specific Energy Sodium-Ion Batteries through Carbon Anode Optimization, Adv. Energy Mater. 8 (17) (2018), https://doi.org/10.1002/aenm.201703268.
- [40] C.A. Bridges, X.G. Sun, J. Zhao, M.P. Paranthaman, S. Dai, In situ observation of solid electrolyte interphase formation in ordered mesoporous hard carbon by

- small-angle neutron scattering, J. Phys. Chem. C 116 (2012) 7701–7711, https://doi.org/10.1021/jp3012393.
- [41] Y. Morikawa, S. Nishimura, R. Hashimoto, M. Ohnuma, A. Yamada, Mechanism of Sodium Storage in Hard Carbon: an X-Ray Scattering Analysis, Adv. Energy Mater. 10 (2020) 1903176, https://doi.org/10.1002/aenm.201903176.
- [42] P. Bai, Y. He, X. Zou, X. Zhao, P. Xiong, Y. Xu, Elucidation of the Sodium-Storage Mechanism in Hard Carbons, Adv. Energy Mater. 8 (15) (2018) 1–9, https://doi. org/10.1002/aenm.201703217.
- [43] H. Kim, et al., Sodium intercalation chemistry in graphite, Energy Environ. Sci. 8 (2015) 2963–2969, https://doi.org/10.1039/c5ee02051d.
- [44] L.F. Zhao, et al., Hard Carbon Anodes: Fundamental Understanding and Commercial Perspectives for Na-Ion Batteries beyond Li-Ion and K-Ion Counterparts, Adv. Energy Mater. 11 (2002704) (2021) 1–28, https://doi.org/ 10.1002/aenm.202002704.
- [45] X. Yi, et al., Unraveling the Mechanism of Different Kinetics Performance between Ether and Carbonate Ester Electrolytes in Hard Carbon Electrode, Adv. Funct. Mater. 32 (2022) 2209523, https://doi.org/10.1002/adfm.202209523.